1 # Numerical investigation into the blasting-induced damage
2 # characteristics of rocks considering the role of in-situ stresses and
3 # discontinuity persistence

4 L.B. Jayasinghe, Junlong Shang[†], Zhiye Zhao, A.T.C. Goh,

5 *Nanyang Centre for Underground Space, School of Civil and Environmental Engineering, Nanyang*
6 *Technological University, Singapore 639798.*

7 †Corresponding author: shangjunlongcsu@gmail.com, jlshang@ntu.edu.sg (J. Shang)

9 **ABSTRACT**

10 This paper presents a 3D coupled Smoothed Particle Hydrodynamics (SPH) and Finite
11 Element Method (FEM) model, which was developed to investigate the extent of damage
12 zone and fracture patterns in rock due to blasting. The RHT material model was used to
13 simulate the blasting-induced damage in rock. The effects of discontinuity persistence and
14 high in-situ stresses on the evolution of blasting-induced damage were investigated. Results
15 of this study indicate that discontinuity persistence and spatial distribution of rock bridges
16 have a significant influence on the evolution of blasting-induced damage. Furthermore, high
17 in-situ stresses also have a significant influence on the propagation of blasting-induced
18 fractures, as well as the patterns of fracture networks. It is also shown that the blasting-
19 induced cracks are often induced along the direction of the applied high initial stresses.
20 Moreover, additional cracks are normally generated at the edges of the rock bridges probably
21 due to the relatively high stress concentration.

22 **Keywords**: Blasting; Rock damage; In-situ stress; Discontinuity persistence; RHT model

23 **1. Introduction**

24 Blasting-induced damage characteristics of rocks is not well understood due to the complex
25 interaction between the blasting induced shock wave and ubiquitous rock discontinuities. An
26 improper blast design may result in inadequate rock fragmentation, or cause unwanted
27 damage of the surrounding rocks or structures, leading to safety and instability issues and
28 economic loss [1-4]. In practice, approximate methods based on experience are mostly used
29 in the prediction and control of blast damage. However, it is necessary to have a better

understanding of the nature and extent of the rock damage caused by blasting to achieve an optimum blasting design by avoiding the negative consequences.

Rock blasting leads to the mechanical deterioration of rock masses and, in particular, results in the opening, loosening and propagating of pre-existing rock discontinuities, as well as the generation of new cracks in rock matrix by the combined actions of the stress wave and the gas pressure. In the process of rock fragmentation by blasting, stress wave is mainly responsible for the initiation of the initial radial fracture network, while the explosion gas pressure further extends the cracks towards the rock fragmentation [5-8].

Numerical approaches provide a tool to investigate the mechanisms of rock blast safely and in detail. Finite element method (FEM) has become one of the promising numerical approaches to study the blasting-induced damage characteristics of rocks. Ma and An [9] investigated the influence of pre-existing joints, loading rate and in-situ stress on the damage characteristics of rock masses under blasting using a two-dimensional FEM model. They found that the fractures induced by blasting were oriented in the direction of the maximum in-situ stress. By using a coupled FEM-DEM approach, the dynamic rock fracturing process of jointed rock masses under blasting was numerically investigated by Wang and Konietzky [10], who concluded that the existence of in-situ stress field caused the non-uniformity of rock fracture. However, no plastic crushed zone was observed in their study because the rock mass was assumed to be elastic. Zhu et al. [11] developed a FEM model for understanding the blasting-induced damage in cylindrical rocks. The effects of loading rate and anisotropic high in-situ stresses on blasting performance and blast-induced damage zones was explored by Yilmaz and Unlu [12] through a 3D FLAC analysis. Zhao et al. [13] studied the blasting-induced fracture expansion of bedded coal using the isotropic and kinematic hardening plasticity material model in LS-DYNA. It was noticed that the distance from the bedding plane and the borehole has a significant influence on fracture patterns. Yi et al. [14] used a 2D plane strain model to investigate the effect of in-situ stresses on the fracturing of rock due to blasting.

In previous studies, 2D plane strain models with an equivalent blast pressure were often used to investigate the crack initiation and propagation in blasting under in-situ stresses. Those 2D analyses, however, cannot incorporate the three-dimensional propagation of the energy from the detonation of explosives. Also, it cannot simulate the vertically propagation of the S-

2

61   waves from the borehole. Therefore, a three-dimensional model that can consider the

62   explosive charge length and the detonation velocity of the explosive will offer more realistic

63   results.

64   Additionally, the impact of the areal persistence, which can reflect the three dimensional

65   nature of rock discontinuities, on the evolution of blasting-induced characteristics is still not

66   well understood. In previous numerical studies, trace length (2D) is often used as an

67   approximation of the 3D areal persistence, and sometimes persistence was conservatively

68   assumed to be 100%, which will inevitably result in a wrong prediction of failure mechanism

69   or fragmentation of rocks [15, 16].

70   The objective of this work is to investigate the effects of in-situ stresses and discontinuity

71   persistence on the blasting-induced damage characteristics of rocks by using a three-

72   dimensional numerical approach. To avoid time-consuming computation, the Smoothed

73   Particle Hydrodynamics (SPH) and Lagrangian FEM mesh is coupled in the study to

74   maintain a good computational efficiency, which will be described in Section 2. In what

75   follows, a brief description of the background on modelling is presented. Then, the

76   calibration and validation of the model parameters to simulate the blasting-induced rock

77   damage are presented. Subsequently, the effects of discontinuity persistence and high in-situ

78   stresses on the damage zone and fracture patterns in rock due to blasting are investigated,

79   followed by the results interpretation, discussion, and conclusion of the study.

80   **2. Numerical model set-up**

81   In this study, the commercial software LS-DYNA [17] and the Riedel-Hiermaier-Thoma

82   (RHT) model [18] was used to simulate the damage evolution of rock mass under blasting

83   load. The detonation of the explosive was directly modelled with the high explosive burn

84   material model with Jones-Wilkins-Lee (JWL) equation of state in LS-DYNA.

85   **2.1 Rock material model**

86   LS-DYNA contains several material models that can be used to represent damage evolution

87   of rock under blasting. The RHT material model, which is capable of characterising rock

88   mass behaviour under high strain rate blast loads, was used in this study. It is an advanced

89   plasticity model for brittle materials such as concrete and rocks. Literature has shown that the

90   RHT material model can successfully incorporate non-linear rock properties [14, 19-21].

91   In the RHT model, the strength model is described using the three limit surfaces in stress

92   space, namely the initial elastic yield surface, the failure surface and the residual surface

93   which consider pressure and strain rate. This model also considers the effect of strain

94   hardening and damage softening to characterise the post-yield and post-failure behaviours

95   [22].

96   The failure surface, σ_f, describes the maximum distortion stress that the material can

97   withstand and it is expressed as,

98
$$\sigma_f = f_c \sigma_f^* \left(p^*, F_r(\dot{\varepsilon}_p, p^*) \right) R_3(\theta, p^*) \tag{1}$$

99   where θ is Lode angle, $\dot{\varepsilon}_p$ is the effective plastic strain rate and p^* is the normalized pressure

100   to the unconfined uniaxial cylindrical compressive strength, f_c. The factor R_3 is introduced to

101   account for the reduced strength on shear and tensile meridians. F_r is the dynamic strain rate

102   increase factor and it is defined by Eqs. (2) to (4).

103
$$F_r(\dot{\varepsilon}_p, p^*) = \begin{cases} F_r^c & 3p^* \geq F_r^c \\ F_r^c - \frac{3p^* - F_r^c}{F_r^c + F_r^t f_t^*}(F_r^t - F_r^c) & F_r^c > 3p^* \geq -F_r^t f_t^* \\ F_r^t & -F_r^t f_t^* > 3p^* \end{cases} \tag{2}$$

104
$$F_r^{c,t}(\dot{\varepsilon}_p) = \begin{cases} \left(\frac{\dot{\varepsilon}_p}{\dot{\varepsilon}_0^{c,t}}\right)^{\beta_{c,t}} & \dot{\varepsilon}_p \leq \dot{\varepsilon}_p^{c,t} \\ \gamma_{c,t} \sqrt[3]{\dot{\varepsilon}_p} & \dot{\varepsilon}_p > \dot{\varepsilon}_p^{c,t} \end{cases} \tag{3}$$

105   $$log\,\gamma_c = 6\beta_c - 0.492; \quad log\,\gamma_t = 7\beta_t - 0.492 \tag{4}$$

106   In the above equations, c and t (subscripts and superscripts) denote compression and tension,

107   respectively. β_c and β_t are the compressive and tensile strain rate dependence exponents,

108   respectively, and f_t^* denotes the normalized tensile strength to the compressive strength, f_c.

109   The initial elastic surface, σ_{el}, is derived from the failure surface, σ_f, using the elastic strength

110   parameter, F_e, and the cap function, F_c, as given in Eq. (5).

111
$$\sigma_{el} = f_c \sigma_f^* \left(\frac{p^*}{F_e}, F_r(\dot{\varepsilon}_p, p^*) \right) R_3(\theta, p^*) F_e(p^*) F_c(p^*) \tag{5}$$

112   When the stress states reach the failure surface, the damage from the plastic strain

113   accumulates as:

114 $$D = \sum \frac{\Delta\varepsilon_p}{\varepsilon_p^f}; \qquad \varepsilon_p^f = D_1(p^* - (1-D)p_t^*)^{D_2} \geq \varepsilon_{f,min} \tag{6}$$

115 where D is the damage, ranging from 0 (undamaged) to 1 (fully damaged), $\Delta\varepsilon_p$ is the

116 accumulated plastic strain, ε_p^f is the equivalent plastic strain at failure, p_t^* is the normalized

117 failure cutoff pressure (often denoted as Hugoniot Tensile Limit) and $\varepsilon_{f,min}$ is the minimum

118 allowable plastic strain. D_1 and D_2 are the constants.

119 After damage begins to accumulate, the failure surface starts soften and then the residual

120 surface, σ_r, is defined as:

121 $$\sigma_r^*(p^*) = \begin{cases} A_f p^{*n_f} & p^* > 0 \\ 0 & p^* \leq 0 \end{cases} \tag{7}$$

122 where A_f and n_f are the constants. A detailed description of the RHT material model can

123 found in Borrvall and Riedel [22].

2.2 Blasting load

125 In numerical simulations, blast loads can be directly applied on the borehole wall as a blast

126 pressure curve can be calculated using empirical equations [23-25]. On the other hand, the

127 blast loads can also be generated by the explosive charge that can be simulated using high

128 explosive burn material model with the JWL equation of state (EOS) in LS-DYNA. The JWL

129 EOS defines the pressure as a function of the relative volume, V and internal energy, E,

130 which can be expressed as [17]

131 $$P = A\left(1 - \frac{\omega}{R_1 V}\right)e^{-R_1 V} + B\left(1 - \frac{\omega}{R_2 V}\right)e^{-R_2 V} + \frac{\omega E}{V} \tag{8}$$

132 where A, B, R_1, R_2 and ω are the material constants.

133 A factor called burn fractions, F, is used in the high explosive burn material model to control

134 the chemical energy release for detonation simulations, and it is calculated as [17]

135 $$F = \max(F_1, F_2) \tag{9}$$

136 $$F_1 = \begin{cases} \frac{2(t-t_l)D}{3\Delta x} & if\ t > t_l \\ 0 & if\ t \leq t_l \end{cases} \tag{10}$$

5

137 $$F_2 = \frac{1-V}{1-V_{cj}}$$ (11)

138 where D is the detonation velocity, ρ is the density, V_{cj} is the Chapman-Jouget relative

139 volume, V is the relative volume, t_l is initiation time, t is the current time and Δx is the

140 characteristic length of an element [17].

2.3 Model parameters and validation

141

142 The results of the laboratory-scale explosion tests in Banadaki [26] were used to calibrate the

143 RHT model and verify the simulation results of this study. Banadaki [26] conducted 30

144 laboratory-scale explosion tests on two different types of cylindrical rock samples

145 (Laurentian granite and Barre granite). In this study, the results based on the Barre granite

146 were chosen in the comparison study. The cylindrical Barre granite sample has a diameter of

147 144 mm and a height of 150 mm, with a 6.45 mm diameter blasthole in the middle as shown

148 in Fig. 1(a). A copper tube with 1.2 mm thick was installed in the blasthole to prevent gas

149 penetration into the cracks.

150 As mentioned earlier, in our simulations, a 3D coupled Smoothed Particle Hydrodynamics

151 and Finite Element Method (SPH-FEM) model is established to investigate the failure

152 mechanisms of rocks under blast loading. The use of the conventional Lagrangian meshes in

153 the large deformation problems will result in mesh tangling, leading to severe numerical

154 instabilities. SPH is a mesh-free Lagrangian method which employs a finite number of

155 particles that carry individual mass to represent the material and form the computational

156 domain. SPH method has a solid ability to deal with dynamic large deformation problems,

157 due to its ability to handle large distortions by avoiding mesh tangling and remeshing.

158 Although SPH has great advantages in simulating many problems in engineering and science,

159 SPH is much expensive in terms of computation time (especially for 3D model). Because a

160 large number of small particles would be required and the time step would become very

161 small. Thus, coupling the SPH and Lagrangian FEM mesh is a potentially right solution to

162 overcome the element distortion, and as well as to maintain good computational efficiency. In

163 this study, SPH algorithm was implemented in LS-DYNA to model the detonation of PETN

164 explosive, and the Lagrangian meshes were used to model the rock and copper tube as shown

165 in Fig. 1(b). The procedure of the RHT model parameter selection has been presented in

166 detail in Xie et al. [19]. The model parameters were adjusted by conducting sensibility

167 analysis. The RHT model parameters for Barre granite are listed in Table 1. The parameters

168 for the PETN explosive are summarized in Table 2. The plasticity kinematic material model

169 was used to model the copper tube, and the material parameters for the copper are given in

170 Table 3.

171

172

173   (a)   (b)
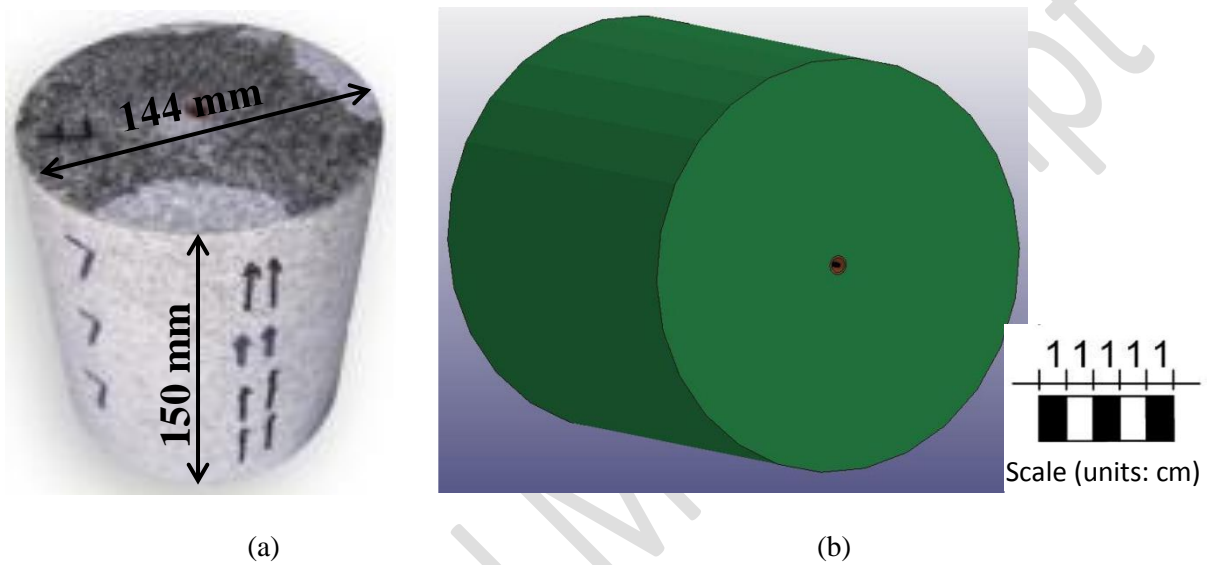
174 **Fig. 1.** Cylindrical Barre granite samples. (a) Blast experiment [26] and (b) 3D numerical model.

175

176 **Table 1.** Material parameters for rock

Parameter	Value	Parameter	Value	Parameter	Value
RO (kg/m^3)	2660	T2	0	EPM	0.01
SHEAR (GPa)	21.9	E0C	3×10^{-8}	AF	0.25
EPSF	2	E0T	3×10^{-9}	NF	0.62
B0	1.22	EC	3×10^{22}	GAMMA	0
B1	1.22	ET	3×10^{22}	A1 (GPa)	25.7
T1 (GPa)	25.7	BETAC	0.032	A2 (GPa)	37.84
A	2.44	BETAT	0.036	A3 (GPa)	21.29
N	0.76	PTF	0.001	PEL (MPa)	125

7

FC (MPa)	167.8	GC*	1	PCO (GPa)	6
FS*	0.18	GT*	0.7	NP	3
FT*	0.05	XI	0.5	ALPHA	1
Q0	0.567	D1	0.04		
B	0.01	D2	1		

177

178 **Table 2.** Material and JWL EOS parameters for PETN [26]

Density (kg/m^3)	Velocity of detonation (m/s)	P_{CJ} (GPa)	A (GPa)	B (GPa)	R_1	R_2	ω	E_0 (GPa)
1320	6690	16	586	21.6	5.81	1.77	0.282	7.38

179

180 **Table 3.** Material parameters for copper [27]

Density (kg/m^3)	Young's modulus (GPa)	Poisson's ratio	Yield stress (MPa)	Tangent modulus (MPa)	β	C (s^{-1})	P
8930	117	0.35	400	100	0	1.346 x 10^6	5.286

181 Figs. 2 and 3 show comparisons of the blasting-induced crack patterns obtained from

182 experiment [26] and the results of the present 3D numerical model. In the numerical results,

183 the cracks are shown by the damage contours which range from 0 to 1. The blue colour

184 represents the fringe level 0 which indicates the undamaged rock, while the red colour

185 represents the fringe level 1 which indicates the rock is completely damaged. The other

186 colours which are associated with fringe levels between 0 and 1 represent the different

187 damage levels of the rock.

188 It can be seen from Figs. 2 and 3 that the results of our 3D model match well with that

189 obtained from experiment. Basically, crush zones are generated around the blastholes and

190 radial cracks propagate towards the outer boundaries from the blastholes when the detonation

191 is occurred. In addition, a few circumferential cracks can be seen close to the boundary of the

192 sample at the bottom surface. The intensity of cracks at the bottom surface of the rock sample

193 is much higher than that observed at the top surface, which is due to the effect of the

8

superposition of stress wave. The observed reasonable predictions of our 3D numerical model give us some confidence in its further application in the later study.
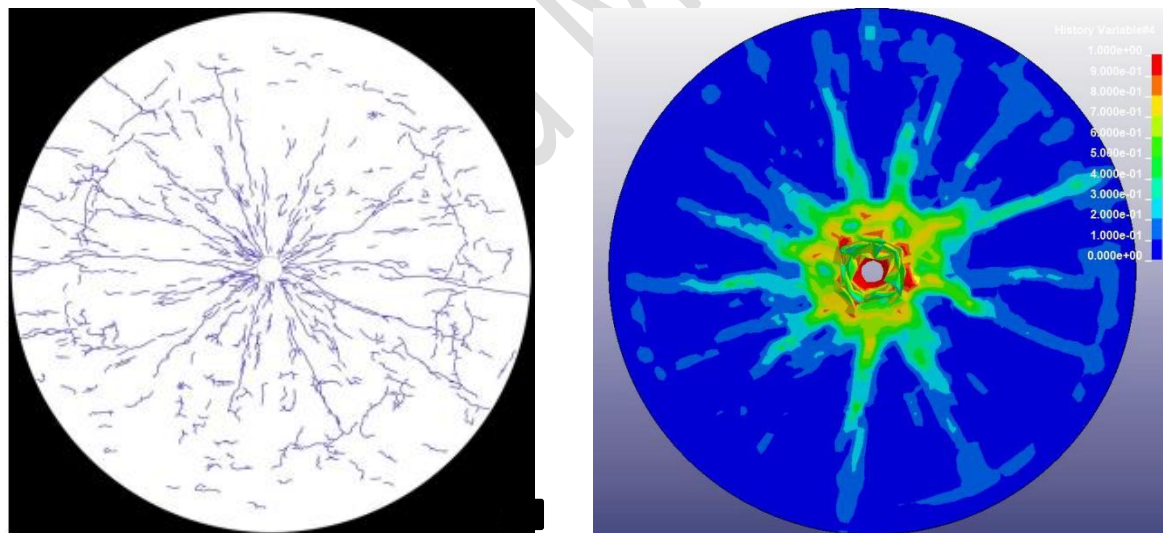

(a)   (b)
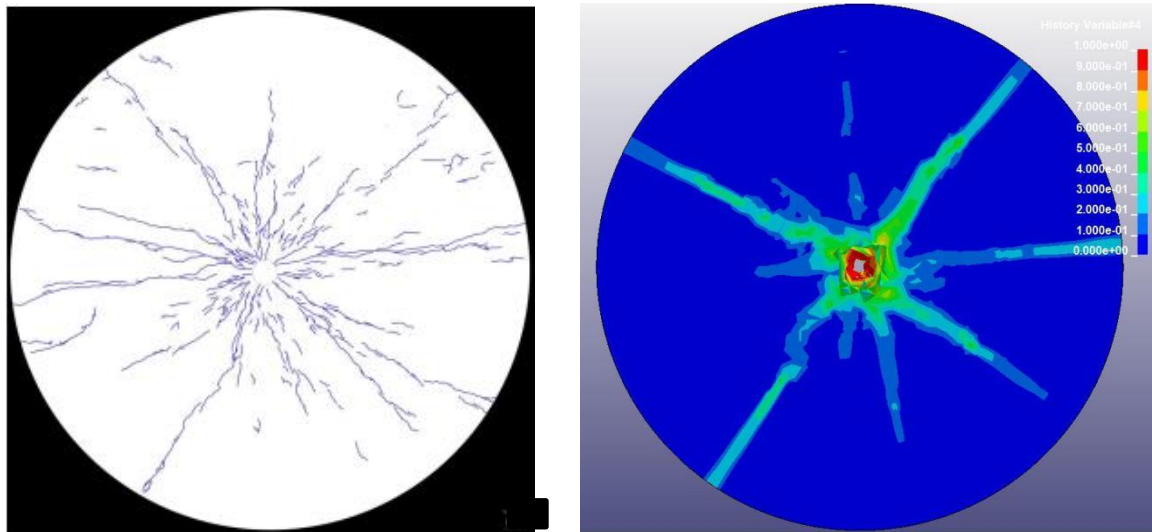
Fig. 2. Comparison of blasting-induced crack patterns observed at the top surface of a cylindrical Barre granite sample. (a) Blast experiment [26] and (b) 3D numerical simulation.


(a)   (b)

Fig. 3. Comparison of blasting-induced crack patterns observed at the bottom surface of a cylindrical Barre granite sample. (a) blast experiment [26] and (b) 3D numerical simulation.

To further testify the generated 3D numerical model, the numerically and experimentally obtained maximum pressures measured at different distances from the borehole wall were

206   compared (Fig. 4). The comparison shows that the present simulation results of pressure
207   distribution match the test results quite well, which further validates the robustness of the
208   proposed 3D SPH-FEM model.
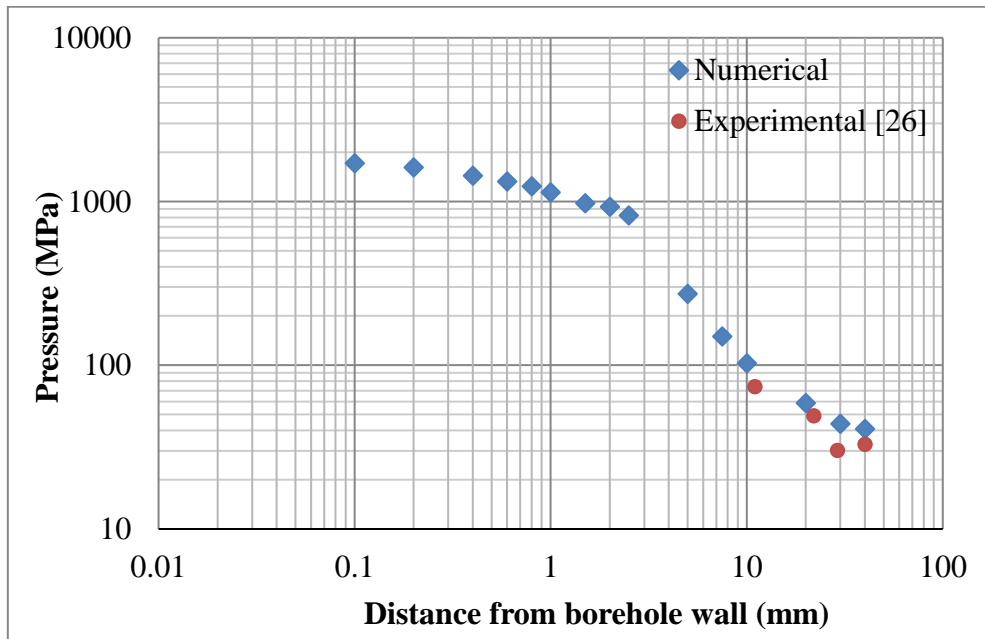
209

210   **Fig. 4.** Comparison of the numerically and experimentally obtained maximum pressures measured at
211   different distances from the borehole walls.

3. Results and discussion

213   In this section, the results of the crack initiation and propagation due to blasting under various

214   scenarios are presented. The influence of in-situ stresses and discontinuity persistence on the

215   characteristics of the blasting-induced damage of rock mass are evaluated and discussed.

216   Fig. 5 shows the developed 3D SPH-FEM model to study the damage mechanisms of rock

217   under blasting. The model is 4 m long, 4 m wide and 2 m high. The blasthole diameter and

218   length are 50 mm and 0.5 m, respectively. The explosive charge was modelled with the SPH

219   particles, while the rock was modelled with the Lagrangian meshes. The rock mass was

220   modelled using RHT material model as described earlier. However, ANFO explosive was

221   considered in these analyses and the parameters for the ANFO explosive are summarized in

222   Table 4. The automatic node to surface contact conditions was used for the coupling

223   interaction between the SPH particles and Lagrange solid elements. Non-reflecting

224   boundaries were applied at the boundaries except the top surface which is free.

225
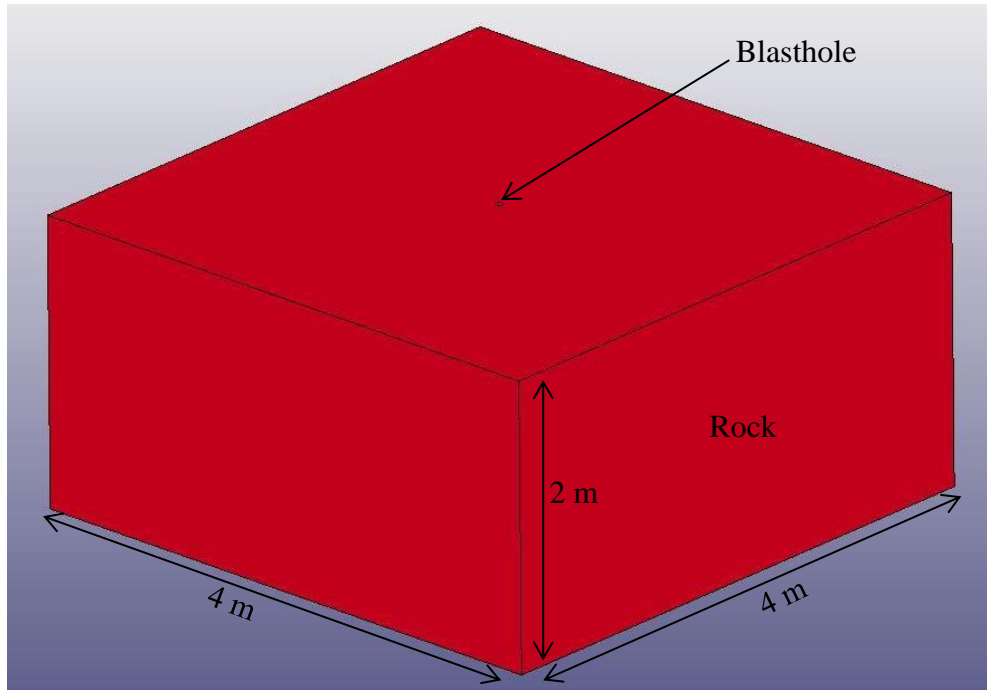
Fig. 5. 3D FE model

Table 4. Material and JWL EOS parameters for ANFO

Density (kg/m^3)	Velocity of detonation (m/s)	P_{CJ} (GPa)	A (GPa)	B (GPa)	R_1	R_2	ω	E_0 (GPa)
931	4160	5.15	49.46	1.891	3.907	1.118	0.333	2.484

3.1 Effect of in-situ stresses on blasting-induced fracture behaviour

The magnitude of in-situ stresses normally increase with the depth. High in-situ stresses at deeper depths can cause difficulties for excavation-related engineering activities such as deep tunnelling and mining. The effect of in-situ stresses on the fracturing of rock due to blasting has been investigated extensively, most of which however were based on the 2D plane strain models with an equivalent pressure-time history curve applied on the borehole wall [6, 9, 12, 14]. In this study, a 3D SPH-FEM coupled model combining blast loads and in-situ stresses is used, which is expected to realistically reflect the three-dimensional nature of the blasting-induced fracturing process in rocks. In order to assess the influence of in-situ stresses on fracture behaviour, four different analysis cases are considered as shown in Fig. 6 and Table 5. Fig. 6 shows the cross-sectional view of the established numerical model. The pressures P1 and P2 were applied to the outer vertical boundaries of the model, and the stress initialization to apply constant initial in situ stresses in the rock was first carried out by using the

11

241   *CONTROL_DYNAMIC_RELAXATION option in LS-DYNA. After the stress

242   initialization, the detonation of the explosive was simulated, and the stress evolution in the

243   rock and the initiation and propagation of blasting-induced cracks were monitored.
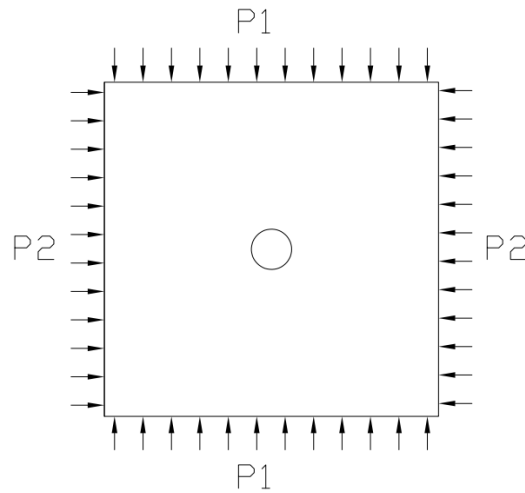

244

245   **Fig. 6.** Cross-sectional view of the established numerical model.

246   **Table 5.** Four analysis cases designed to understand the effects of in-situ stresses on fracture

247   behaviour

Analysis case	P1 (MPa)	P2 (MPa)
I	0	0
II	60	60
III	60	30
IV	60	0

248   Fig. 7 illustrates the initiation and propagation of cracks around the blasthole at different

249   times for case I. It can be seen that just after the detonation of the explosive initiated at the

250   bottom of the blasthole, a crushed zone is first developed continuously around the blasthole

251   as shown in Fig. 7(a). Then, radial cracks were induced by the tensile stress and propagated

252   radially, as shown in Figs. 7(b) and (c). As can be seen in Fig. 7(c), the blasting damage of

253   rock gradually evolved from the bottom of the blasthole to the top surface. As a result of the

254   reflection of the stress wave at the top free surface and thus generation of excessive tensile

255   stresses, the damage is more significant at the top surface.

256

257   (a)   (b)

258

259   (c)   (d)
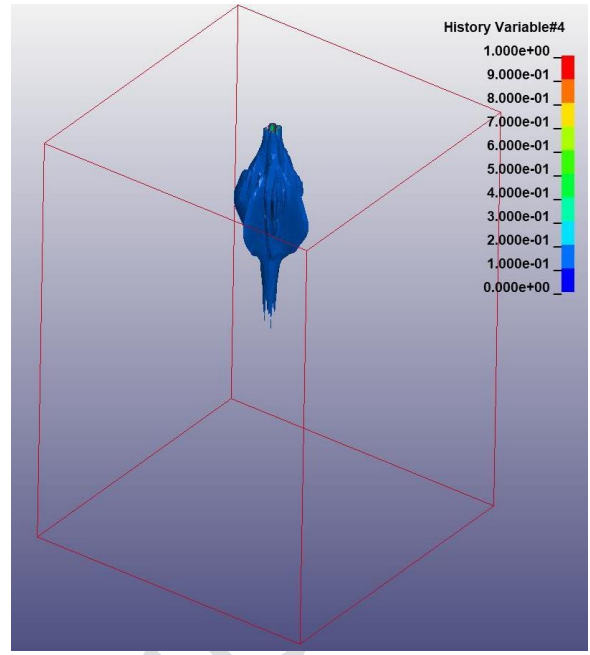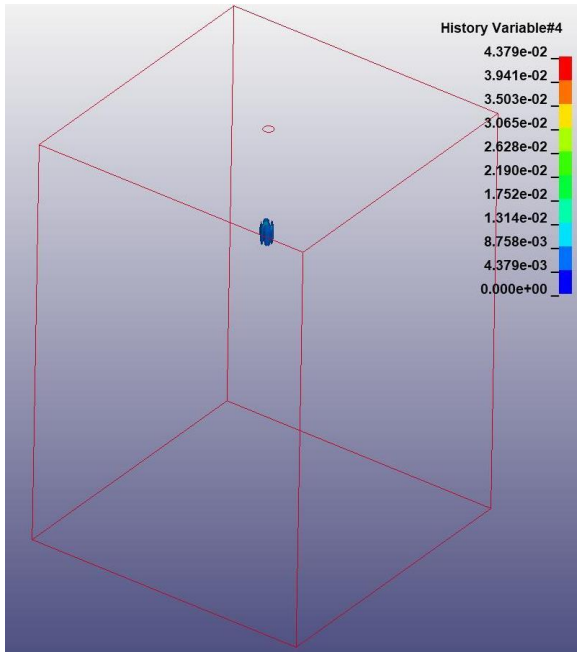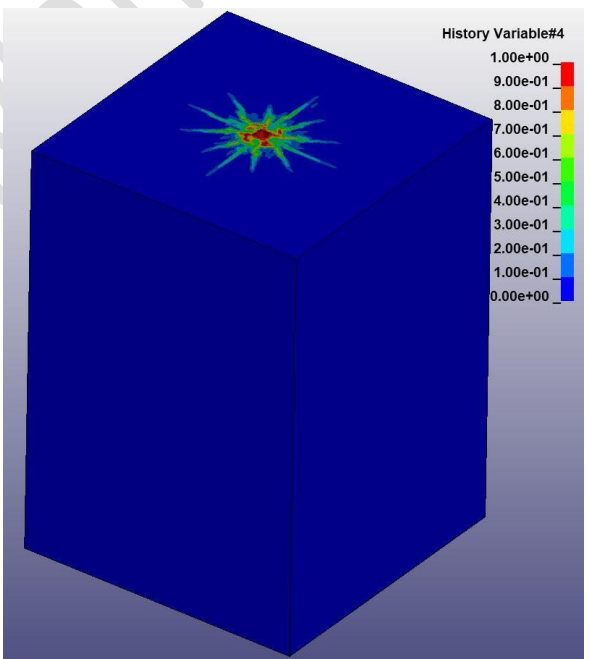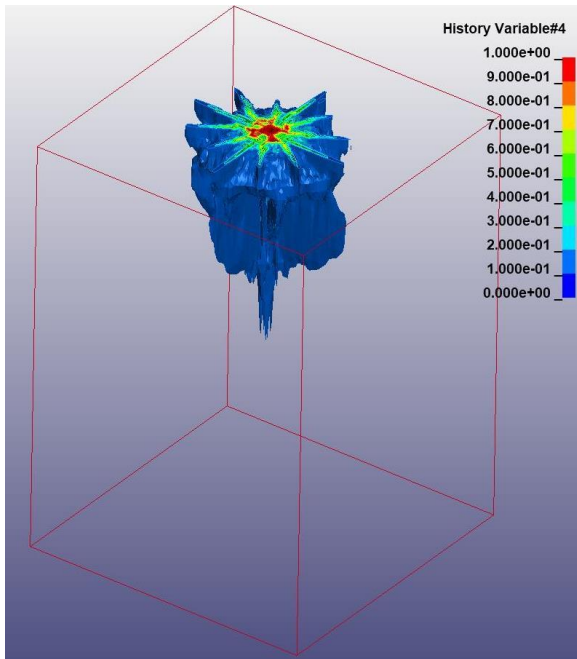
Fig. 7. Evolution of blasting-induced cracks at times. (a) 10 μs (b) 100 μs (c) 400 μs and (d) crack pattern at the top surface at 400 μs.

Fig. 8 shows a comparison of the blasting-induced rock damage on the top surface for all cases. The comparison of the results obtained in cases I and II shows that the rock mass

264 without the influence of horizontal in-situ stresses (case I) exhibits more blasting-induced
265 damage than the case with the consideration of horizontal in-situ stresses (case II). The extent
266 of cracks is expected to decrease with increasing the lateral in-situ stresses, because the stress
267 (or confinement) applied on the rock tends to resist the propagation of blasting-induced
268 fractures. Also, it can be clearly seen that when there is an anisotropic in-situ stress field, the
269 rock mass is subjected to anisotropic rock damage, and blasting-induced cracks are aligned in
270 the direction of the major horizontal principal stress axis (i.e. the direction of P1 in this study).
271 This is due to the suppression of the tensile stress in the direction of P2 under a higher P1.
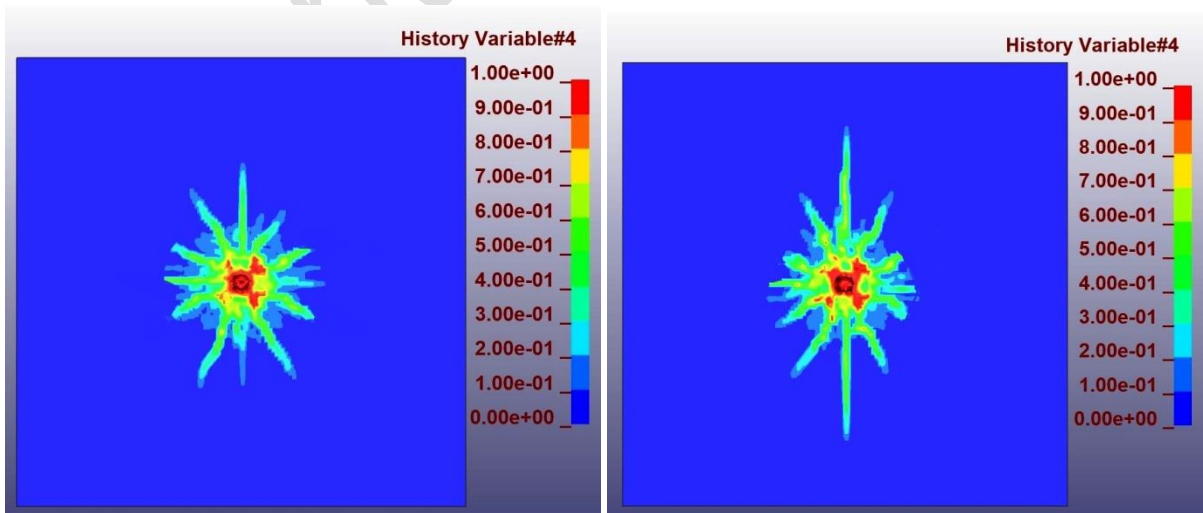272 The results agree well with some numerical findings in literature [6, 9, 12, 14].

273

274 (a)   (b)

275

276 (c)   (d)

14
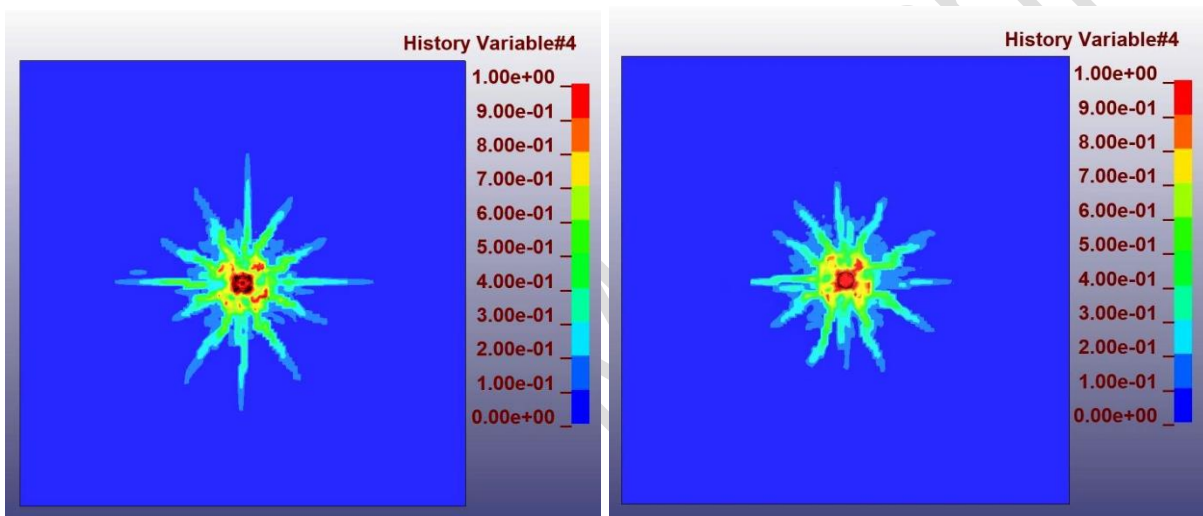
277   **Fig. 8.** Crack patterns on the top surface for (a) case I (b) case II (c) case III and (d) case IV.

278   As stated above, there exist many 2D studies on the influence of in-situ stress on blast-

279   induced rock cracks in literature. It is seen that the present 3D numerical results agree well

280   with some of previous numerical findings. A comparison study was further carried out to

281   understand the difference between the results from 3D and 2D simulations. The blasting-

282   induced rock damage on the top surface obtained from the 2D and 3D models are compared

283   in Fig. 9. Although the crack patterns are similar for both models, the blasting-induced rock

284   cracks obtained from the 3D analysis are relatively larger, because of the effect of the stress

285   wave superposition when the detonation wave propagation within the cylindrical charge.

286   Within the acceptable computation time, the 3D model predicts the cracking behaviour more

287   realistically, because it considers the explosive charge length and velocity of detonation of

288   the explosive.

289

290   (a)   (b)
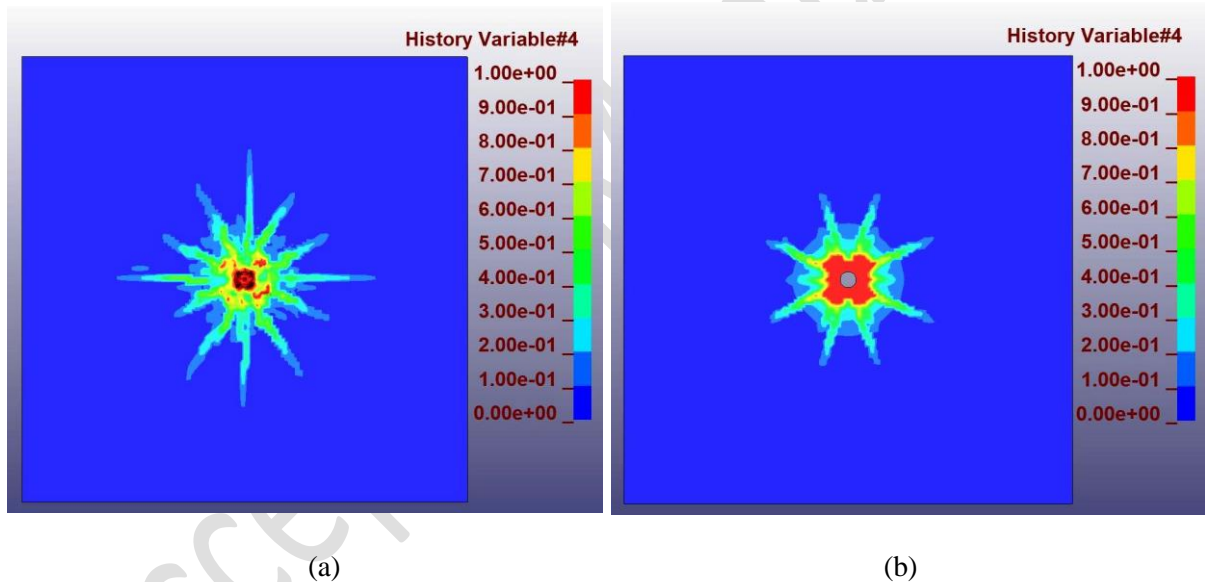
291   **Fig. 9.** Crack patterns on the top surface from (a) 3D analysis and (b) 2D analysis.

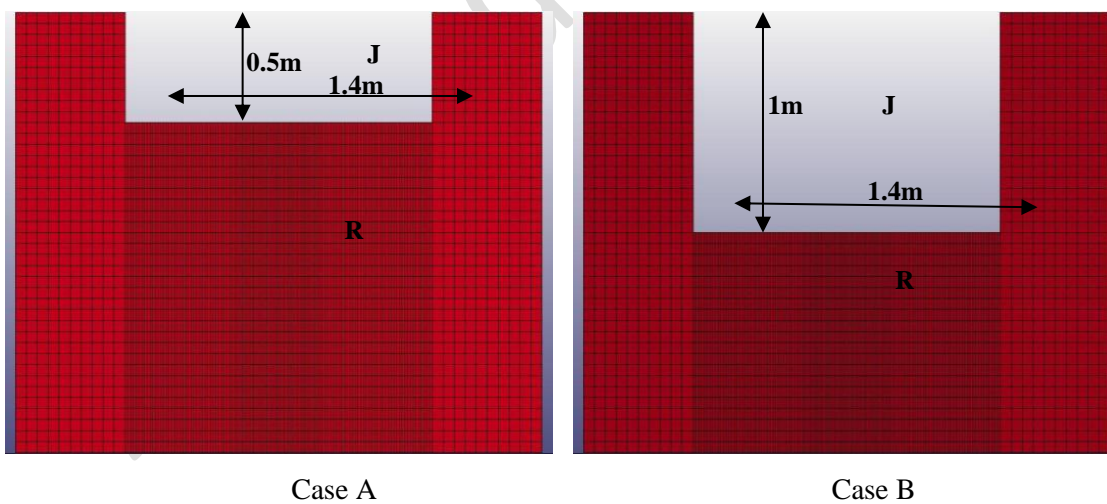292   **3.2 The role of discontinuity persistence**

293   Rock discontinuities are ubiquitous in nature, which can unavoidably influence the blasting-

294   induced fracture propagation in natural rocks. The term discontinuity persistence, k, has been

295   used to describe the areal extent of a rock discontinuity. It is defined as the fraction of

296   continuous discontinuity area, as expressed by Eq. 12 [28].

297    $$k = \frac{A_j}{A_j + A_b} \tag{12}$$

298 where A_j is the total area of joints along the joint plane and A_b is the total area of rock bridges.

299 The small area of intact rock separating coplanar or non-coplanar joints is defined as a rock

300 bridge [29], which rock bridge plays an important role in stabilizing jointed rock masses [30,

301 31].

302 To assess the influence of discontinuity persistence and geometry of rock bridges on the

303 blasting-induced fracture behaviour, four different cases are considered. Fig. 10 shows the

304 configurations of the continuous joint segments (marked by "J") and rock bridges (marked by

305 "R") along the joint plane for each analysis case. The discontinuity persistence varied from

306 0.18 to 0.36 in this study. The cases A and C have the persistence of 0.18 and for cases B and

307 D it is 0.36 and 0.2, respectively. The distance to the joint plane from the blasthole was taken

308 as 0.2 m. The continuous joint segments were simplified as flat gaps (or fissures) with a

309 width of 2 mm and no filling material was considered in the simulations. A surface to surface

310 contact type was applied to simulate the joint plane, without the need of assigning joint

311 stiffness, roughness parameters. It is also assumed that the true cohesion of the continuous

312 joint segments is negligible, because the tensile and shear strengths of the intervened rock

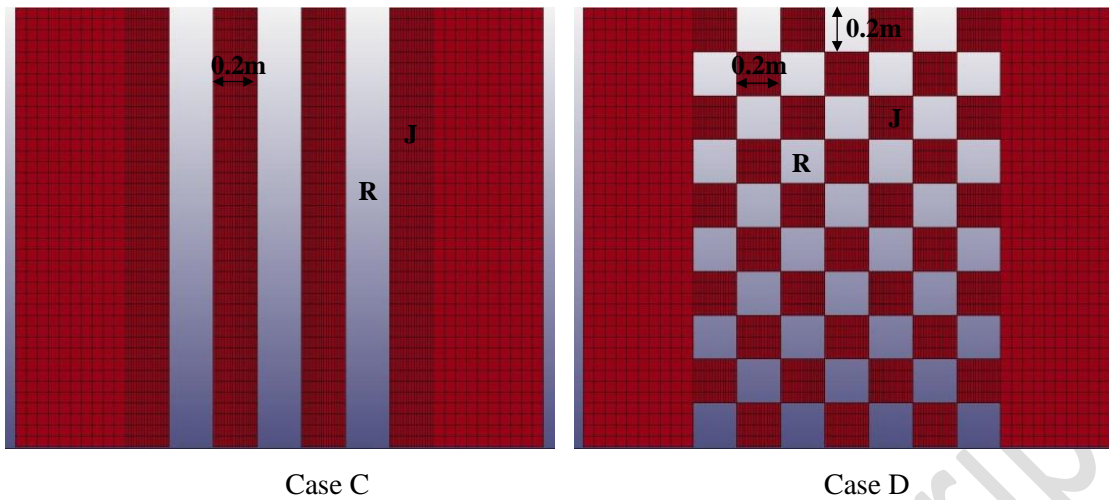313 bridges can be much larger than that of joint segments.

314

315

316   Case A   Case B

16

317

318   Case C   Case D

Fig. 10. Analysis cases used for investigating the effect of discontinuity persistence on blasting-
induced fracture behaviour.

The simulated fracture patterns and damage contours for case A are shown in Fig. 11. Many
blasting-induced cracks were generated around the blasthole and in the region immediately
around the joint plane, as shown in Fig. 11(a). No damage on the rock matrix can be seen
beyond the joint plane in this case. The perspective view of blasting-induced damage on rock
mass is shown in Fig. 11(b). Due to the significant stress concentration around the rock
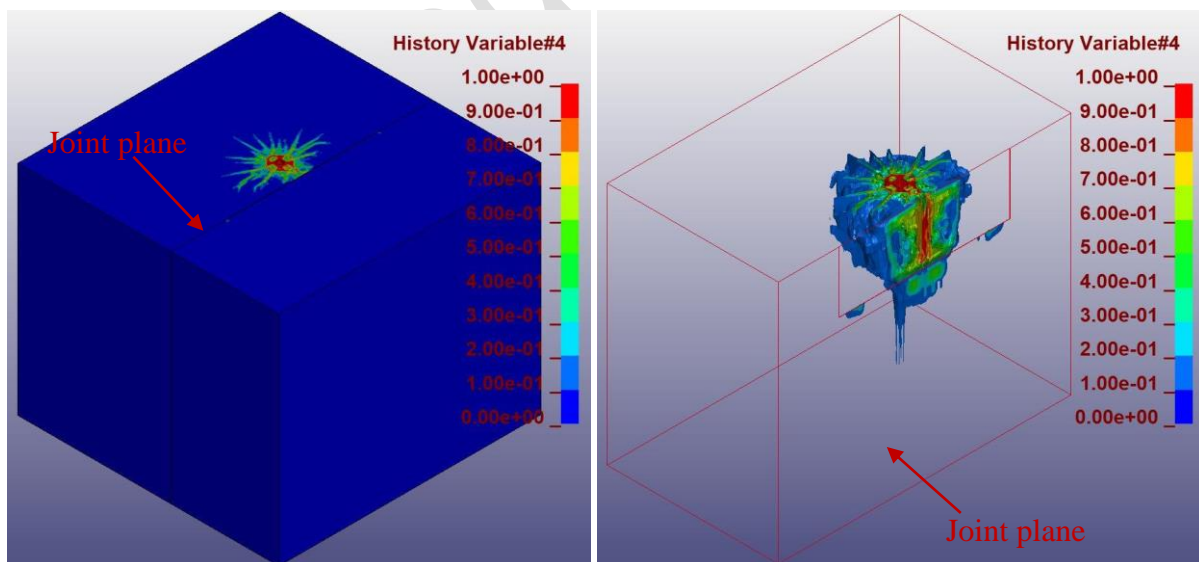bridges, additional damage was created at the edges of the rock bridges

327

328   (a)   (b)

Fig. 11. Blasting-induced damage pattern for case A. (a) on the top surface and (b) perspective view.

17

330 Fig. 12 compares the damage contours on the top surface and the joint plane for cases A and

331 B. It can be clearly seen that there is no additional damage at the edges of the rock bridges in

332 case B. This is due to very little or negligible stress concentration around the rock bridges in

333 case B for the considered intensity of detonation. This indicates that the size of the joints has

334 a significant influence on the expansion of the crack networks in the rock mass.
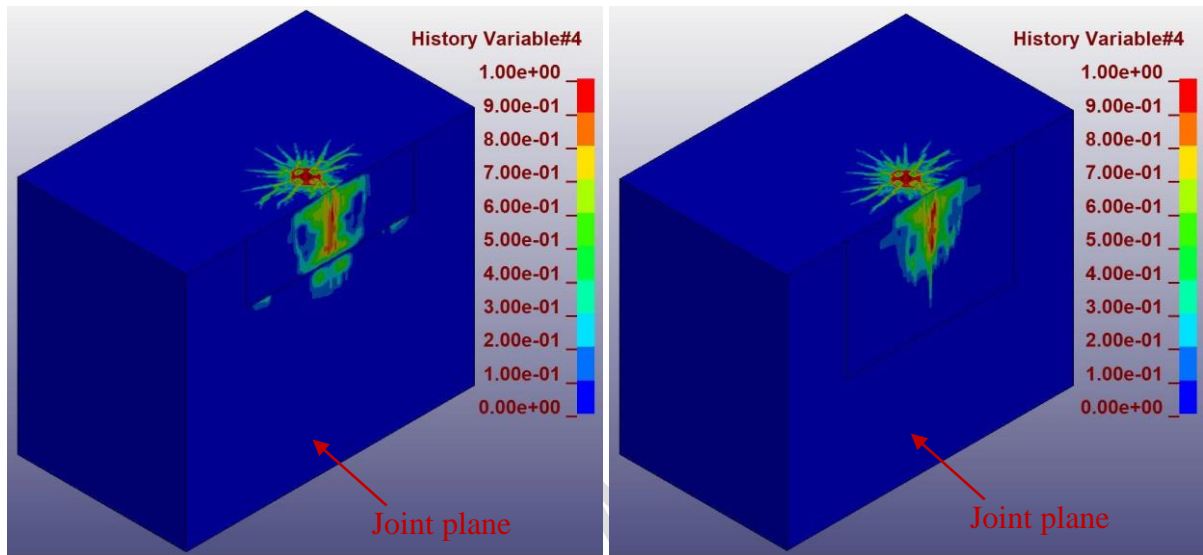
335


336 (a)   (b)

337 **Fig. 12.** Crack pattern on the top surface and on the joint plane for (a) case A and (b) case B.

338 The fracturing patterns and damage contours for cases C and D are shown in Figs. 13 and 14.

339 The results show that the blasting-induced damage in rock is controlled by the joint

340 persistence as well as the spatial location of the rock bridges. There are many blasting-

341 induced cracks can be seen in the region immediately around the joint plane in all the cases

342 and these cracks are mainly generated by tensile failure. This is due to the blasting-induced

343 stress wave reflects at the joint plane, and the reflected stress wave exceeds the dynamic

344 tensile strength of the rock at these locations. Although there are no cracks beyond the joint

345 plane in cases A and B, few new cracks were generated beyond the joint plane in cases C and

346 D, as shown in Figs. 13(a) and 14(a). Moreover, additional damage can be seen at the edges

347 of the rock bridges due to the envisaged significant stress concentration at these locations

348 when the blasting-induced stress wave hits the rock bridges. This indicates that the rock

349 bridge location has a significant influence on the expansion of the crack networks in the rock

350 mass.

18
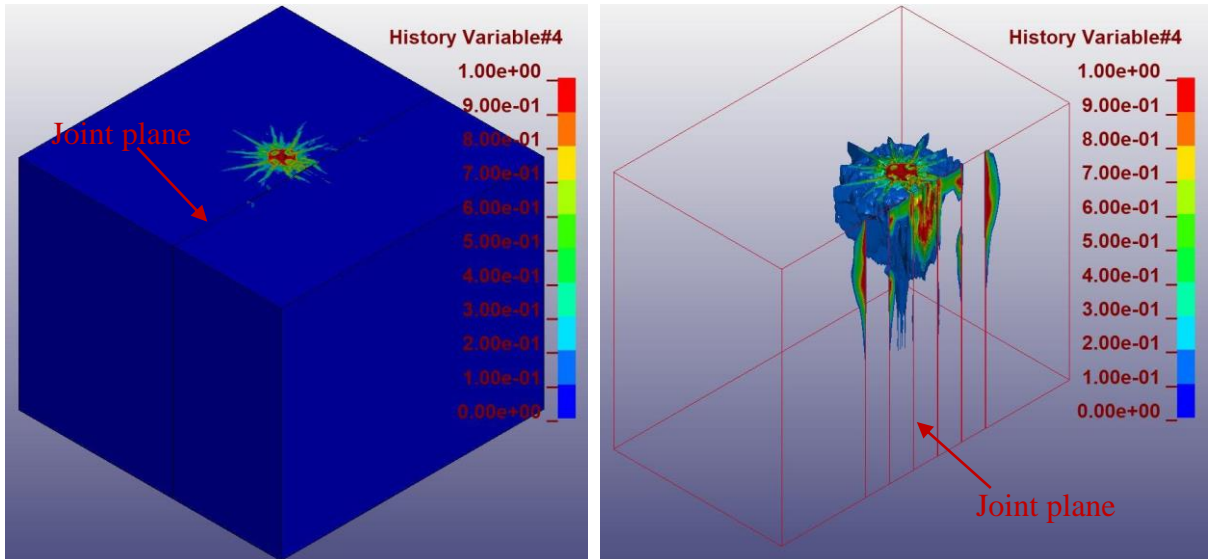
351

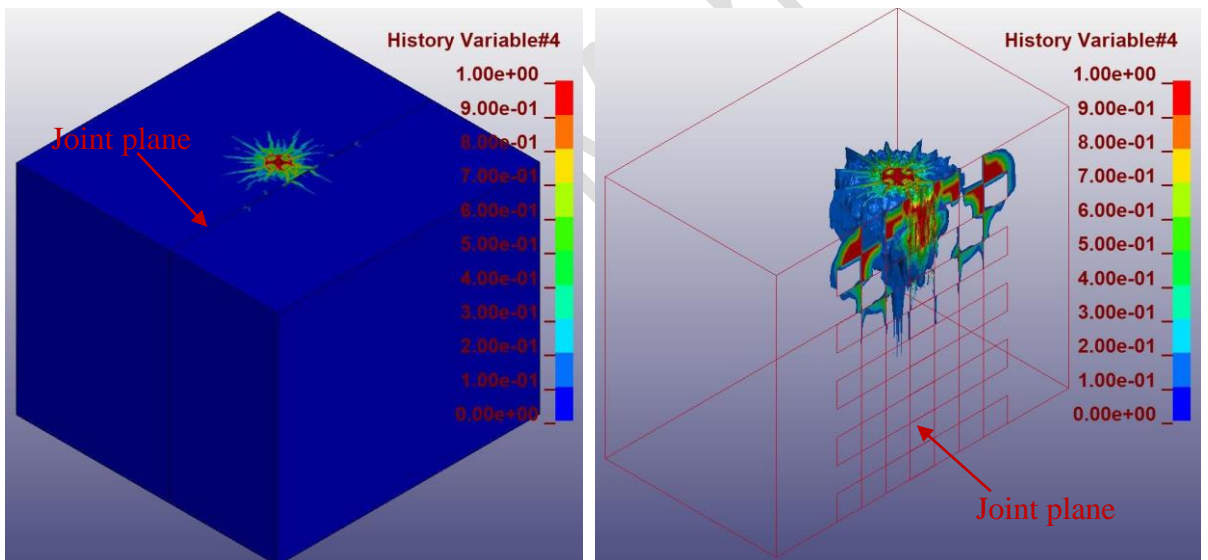352 (a)   (b)

353 **Fig. 13.** Crack pattern for case C. (a) on the top surface and (b) perspective view.

354

355 (a)   (b)

356 **Fig. 14.** Crack pattern for case D. (a) on the top surface and (b) perspective view.

357 **3.3 Fracture characteristics of rocks with different explosives**

358 In order to investigate the effect of explosive types on fracture characteristics, three models

359 were created with different explosives in the blasthole. The first model considers the ANFO

360 explosive detonation in the blasthole (case 1), and the other two models include the

361 detonation of TNT and Emulsion explosives, respectively (case 2 and 3). TNT is the most

362 powerful explosive among them and when it explodes it releases a large amount of energy

363 with a high velocity. For comparison, TNT, Emulsion and ANFO contain detonation energy

364 per unit volume of 7×10^6, 3.87×10^6 and 2.484×10^6 kJ/m^3, respectively. The other important

365 parameter to simulate the power of the detonation of the explosive is the velocity of

366 detonation which is the speed of the detonation shock wave travels through the explosives.

367 TNT has a detonation velocity of 6930 m/s compared to 5122 m/s for the Emulsion and 4160

368 m/s for ANFO. The material parameters for TNT and Emulsion explosives are described in

369 Table 6.

370 **Table 6.** Material and JWL EOS parameters for TNT and Emulsion [14, 32]

| Explosive	Density (kg/m^3)	Velocity of detonation (m/s)	P_{CJ} (GPa)	A (GPa)	B (GPa)	R_1	R_2	ω	E_0 (GPa)
TNT	1630	6930	21	371	3.23	4.15	0.95	0.3	7
Emulsion	1180	5122	9.53	276.2	8.44	5.2	2.1	0.5	3.87

371

372 Figs. 15 and 16 show the fracture patterns and damage contours obtained from the three

373 models. By comparing the results obtained in each case, it can be seen that the top surface of

374 the rock mass is subjected to extensive damage when TNT explosive detonated in the

375 blasthole. On the other hand, it induced less damage below the ground surface. At depths,

376 extensive blasting-induced damage can be seen in case 1 compared to other two cases.

377 Furthermore, when the blasting pressure is high, the crushed zone clearly increases. Because

378 most of energy is spent to create the crushed zone around the blasthole. In drill and blast

379 method, blasting is considered productive when it creates long radial cracks and uniform

380 damage along the length of blasthole. Thus, by comparing the results obtained in each case, it

381 is clear that the use of ANFO which has low blasting pressure and velocity of detonation will

382 help to improve the efficiency of blasting operation.
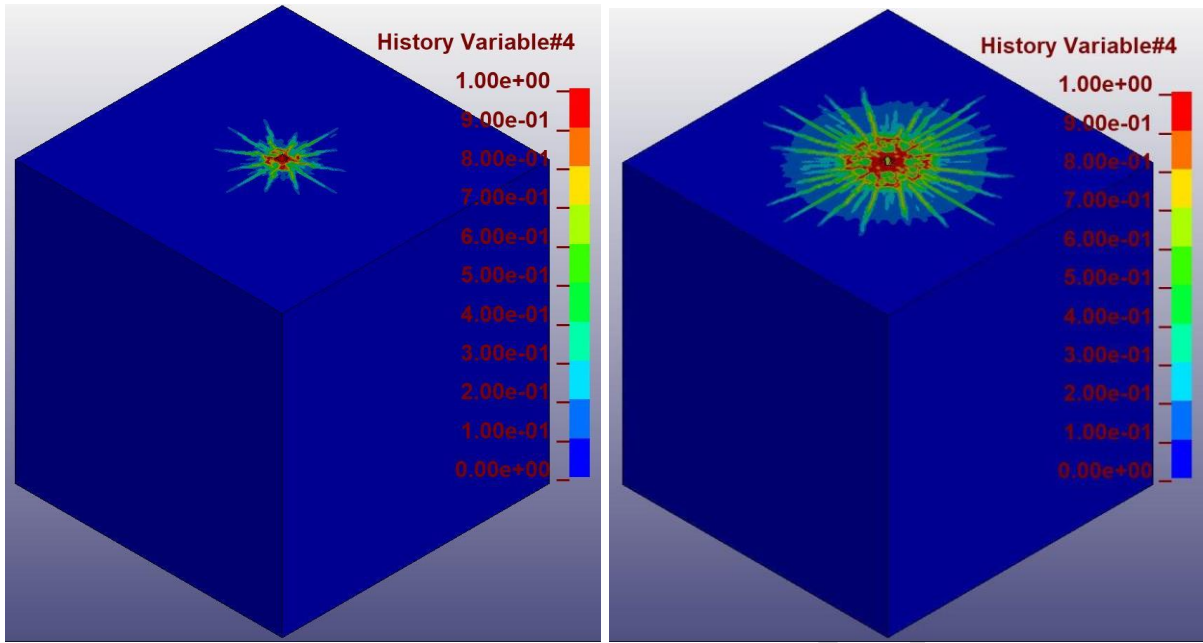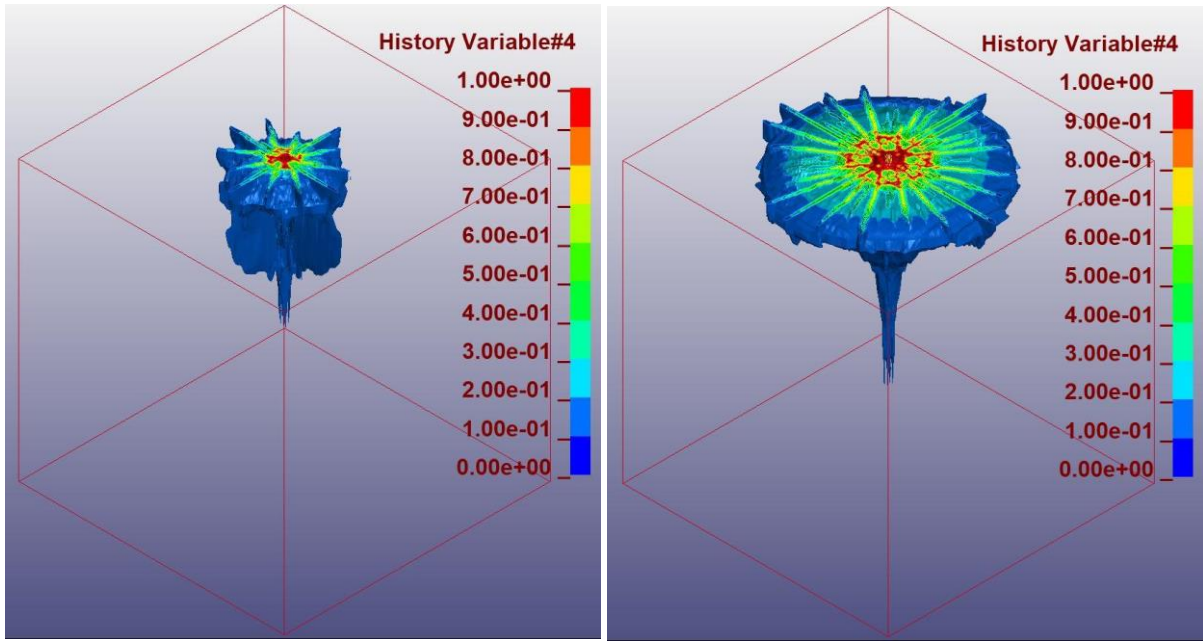
383

384 (a) (b)
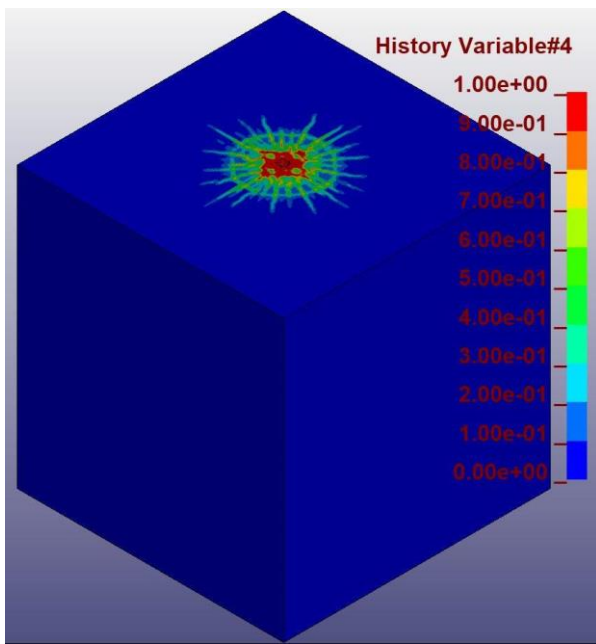
385

386 (c)

387 **Fig. 15.** Crack patterns observed on the top surface for (a) case 1 - ANFO (b) case 2 - TNT (c) case 3

388 - Emulsion

389

390   (a)   (b)
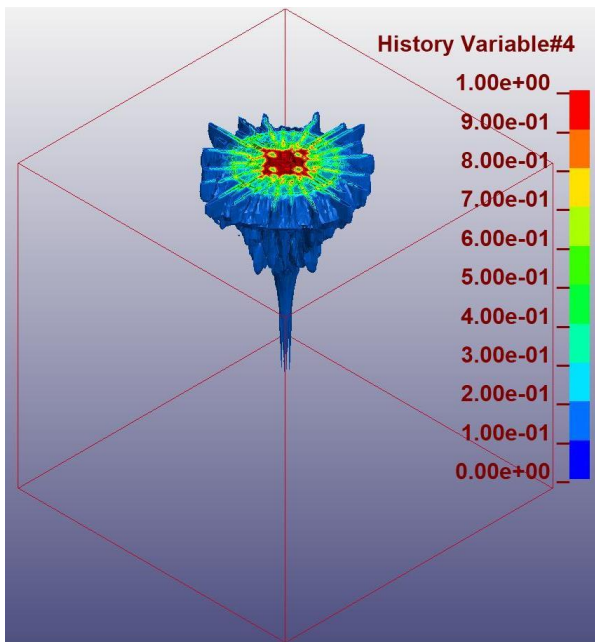
391

392   (c)

393 **Fig. 16.** Perspective view of blasting-induced rock damage for (a) case 1 - ANFO (b) case 2 - TNT

394 (c) case 3 - Emulsion

395 **4. Conclusion**

396 A comprehensive numerical investigation of the effect of in-situ stress and discontinuity

397 persistence on the blasting-induced damage characteristics of rocks was conducted based on

22

398 an established 3D SPH-FEM model. Since 2D analyses cannot incorporate the three-
399 dimensional propagation of the energy from the detonation of the explosive, the fully coupled
400 3D SPH-FEM model was therefore developed, which considers both computation efficiency
401 and modeling accuracy. The model was calibrated and validated against available
402 experimental results in literature. The effects of discontinuity persistence, high in-situ stresses,
403 and magnitude of blast pressures on the evolution of blasting-induced damage were studied.
404 Based on the numerical simulation results, the following conclusions can be drawn.

405   1. The extent of blasting-induced cracks decreases with increasing the lateral in-situ
406   stresses. The results of this study also show that the blasting-induced cracks are
407   oriented in the direction of the high principal stress.

408   2. The blasting-induced damage in the rock is controlled by the joint persistence and the
409   location of the rock bridges. Extensive blasting-induced cracks are generated around
410   the blastholes and in the regions around the joint planes, because the blasting-induced
411   stress wave reflects from the top free surface and produces more tensile stress wave.
412   When the blasting-induced stress wave hits the rock bridges, additional cracks are
413   generated at the edges of the rock bridges due to the high stress concentration at those
414   locations.

415   3. It creates a larger crushed zone when the blasting pressure is high; however, when it is
416   low, it creates long radial cracks and uniform damage along the length of the
417   blastholes. This means that the use of the explosive like ANFO, which has low
418   blasting pressure and velocity of detonation, will help to improve the efficiency of
419   blasting operation.

420 **References**

421 [1]   S. P. Singh and P. Xavier, "Causes, impact and control of overbreak in underground
422   excavations," *Tunnelling and Underground Space Technology,* vol. 20, pp. 63-71,
423   2005.

424 [2]   H. K. Verma, N. K. Samadhiya, M. Singh, and V. V. R. Prasad, "Blast induced
425   damage to surrounding rock mass in an underground excavation," *Journal of*
426   *Geological Resource and Engineering,* vol. 2, pp. 13-19, 2014.

427   [3]   M. F. Hossaini, M. Mohammadi, J. Ghadimi, and A. Abbasi, "Causes of overbreak in
428   tunneling: A case study of Alborz tunnel," in *16th Coal Operators' Conference*,
429   University of Wollongong, 2016, pp. 127-131.

430   [4]   A. Daraei and S. Zare, "Prediction of overbreak depth in Ghalaje road tunnel using
431   strength factor," *International Journal of Mining Science and Technology,* vol. 28, pp.
432   679-684, 2018.

433   [5]   H. P. Rossamanith, K. Uenishi, and N. Kouzniak, "Blast wave propagation in rock
434   mass - Part I: monolithic medium," *International Journal of Blasting and*
435   *Fragmentation,* vol. 1, pp. 317-359, 1997.

436   [6]   F. V. Donze, J. Bouchez, and S. A. Magnier, "Modeling fractures in rock blasting,"
437   *International Journal of Rock Mechanics and Mining Sciences,* vol. 34, no. 8, pp.
438   1153-1163, 1997.

439   [7]   E. Hamdi, N. B. Romdhane, and J. M. L. Cleach, "A tensile damage model for rocks:
440   Application to blast induced damage assessment," *Computers and Geotechnics,* vol.
441   38, no. 2, pp. 133-141, 2011.

442   [8]   H. M. An, H. Y. Liu, H. Han, H. Zheng, and X. G. Wang, "Hybrid finite-discrete
443   element modelling of dynamic fracture and resultant fragment casting and muck-
444   piling by rock blast," *Computers and Geotechnics,* vol. 81, pp. 322-345, 2017.

445   [9]   G. W. Ma and X. M. An, "Numerical simulation of blasting-induced rock fractures,"
446   *International Journal of Rock Mechanics and Mining Sciences,* vol. 45, pp. 966-975,
447   2008.

448   [10]   Z. L. Wang and H. Konietzky, "Modelling of blast-induced fractures in jointed rock
449   masses," *Engineering Fracture Mechanics,* vol. 76, pp. 1945-1955, 2009.

450   [11]   Z. Zhu, H. Xie, and B. Mohanty, "Numerical investigation of blasting-induced
451   damage in cylindrical rocks," *International Journal of Rock Mechanics and Mining*
452   *Sciences,* vol. 45, pp. 111-121, 2008.

453   [12]   O. Yilmaz and T. Unlu, "Three dimensional numerical rock damage analysis under
454   blasting load," *Tunnelling and Underground Space Technology,* vol. 38, pp. 266-278,
455   2013.

456 [13] J.-J. Zhao, Y. Zhang, and P. G. Ranjith, "Numerical simulation of blasting-induced
457   fracture expansion in coal masses," *International Journal of Rock Mechanics and*
458   *Mining Sciences,* vol. 100, pp. 28-39, 2017.

459 [14] C. Yi, D. Johansson, and J. Greberg, "Effects of in-situ stresses on the fracturing of
460   rock by blasting," *Computers and Geotechnics,* vol. 104, pp. 321-330, 2018.

461 [15] J. Shang, "Persistence and tensile strength of incipient rock discontinuities", PhD
462   thesis, the University of Leeds, United Kingdom, 2016.

463 [16] J. Shang, S.R. Hencher, L.J. West, and K. Handley, "Forensic excavation of rock
464   masses: a technique to investigate discontinuity persistence", *Rock Mechanics and*
465   *Rock Engineering,* vol. 50, no. 11, pp. 2911-2928, 2017.

466 [17] LSTC, "LS-DYNA theory manual," ed. Livermore Software Technology Corporation,
467   2006.

468 [18] W. Riedel, K. Thoma, S. Hiermaier, and E. Schmolinske, "Penetration of reinforced
469   concrete by BETA-B-500 numerical analysis using a new macroscopic concrete
470   model for hydrocodes," in *9th International Symposium on the Effects of Munitions*
471   *with Structures*, 1999.

472 [19] L. X. Xie, W. B. Lu, Q. B. Zhang, Q. H. Jiang, M. Chen, and J. Zhao, "Analysis of
473   damage mechanisms and optimization of cut blasting design under high in-situ
474   stresses," *Tunnelling and Underground Space Technology,* vol. 66, pp. 19-33, 2017.

475 [20] S. Jeon and T. Kim, "Characteristics of crater formation due to explosives blasting in
476   rock mass," *Geomechanics and Engineering,* vol. 9, no. 3, pp. 329-344, 2015.

477 [21] K. Liu, Q. Li, C. Wu, X. Li, and J. Li, "A study of cut blasting for one-step raise
478   excavation based on numerical simulation and field blast tests," *International Journal*
479   *of Rock Mechanics and Mining Sciences,* vol. 109, pp. 91-104, 2018.

480 [22] T. Borrvall and W. Riedel, "The RHT concrete model in LS-DYNA," in *The 8th*
481   *European LS-DYNA Users Conference*, Strasbourg, 2011.

482 [23] M. A. Cook, *The Science of High Explosives*. Einhold Publishing Corp, 1958.

483 [24] Q. Liu and P. Tidman, "Estimation of the dynamic pressure around a fully loaded
484   blasthole," in "Technical Report MRL 95-014, CANMET/MRL:15," 1995.

485 [25] J. Dai, *Dynamic Behaviours and Blasting Theory of Rock*. Metallurgical Industry
486   Press, 2002.

487 [26] M. M. D. Banadaki, "Stress-wave induced fracture in rock due to explosion action,"
488   Ph.D thesis, Department of Civil Engineering, University of Toronto, 2010.

489 [27] S. Koneshwaran, D.P. Thambiratnam, and Gallage C, " Performance of buried tunnels
490   subjected to surface blast incorporating fluid structure interaction," *Journal of*
491   *Performance of Constructed Facilities*, vol. 29, no. 3, 2014.

492 [28] H. H. Einstein, D. Veneziano, G. B. Baecher, and K. J. O'Reilly, "The effect of
493   discontinuity persistence on rock slope stability," *International Journal of Rock*
494   *Mechanics and Mining Sciences and Geomechanics Abstracts,* vol. 20, no. 5, pp. 227-
495   236, 1983.

496 [29] J. Shang, Z. Zhao, J. Hu, and K. Handley, "3D particle-based DEM investigation into
497   the shear behaviour of incipient rock joints with various geometries of rock bridges,"
498   *Rock Mechanics and Rock Engineering,* vol. 51, no. 11, pp. 3563-3584, 2018.

499 [30] B. H. Kim, M. Cai, P. K. Kaiser, and H. S. Yang, "Estimation of block sizes for rock
500   masses with non-persistent joints," *Rock Mechanics and Rock Engineering,* vol. 40,
501   no. 2, pp. 169-192, 2007.

502 [31] J. Shang, J.L. West, S.R. Hencher, and Z. Zhao, "Geological discontinuity
503   persistence: implications and quantification," *Engineering Geology,* vol. 241, pp. 41-
504   54, 2018.

505 [32] E. Lee, M. Finer, and W. Collins, JWL equation of state coefficients for high
506   explosives, Lawrence Livermore Laboratory, University of California, 1973.